IET Radar, Sonar & Navigation
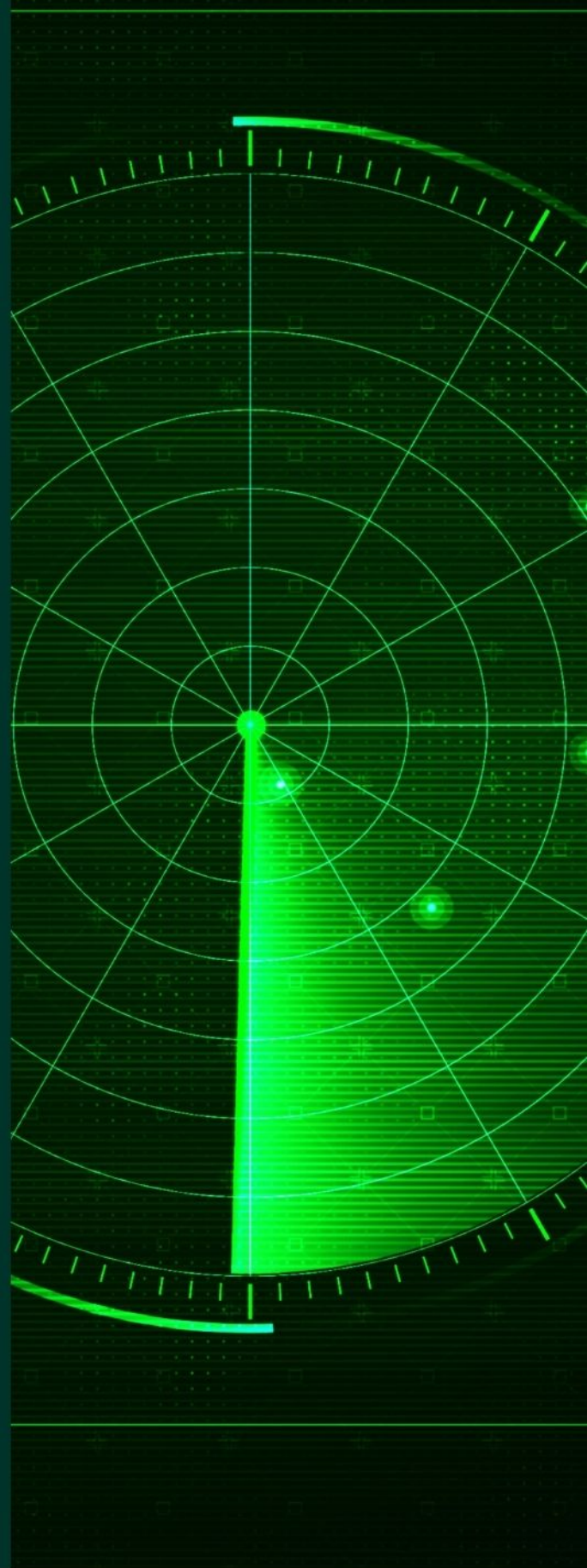
Special Issue Call for Papers

Be Seen. Be Cited. Submit your work to a new IET special issue

Connect with researchers and experts in your field and share knowledge.

Be part of the latest research trends, faster.

Read more

IET The Institution of Engineering and Technology

IET Radar, Sonar & Navigation

The Institution of Engineering and Technology WILEY

ORIGINAL RESEARCH

A cross-cross-correlation based method for joint coregistration of rotated multitemporal synthetic aperture radar images

Laura Parra Garcia[1] | **Luca Pallotta**[2] | **Carmine Clemente**[1] | **Gaetano Giunta**[3] | **John J. Soraghan**[1]

[1]Department of Electronic and Electrical Engineering, University of Strathclyde, Glasgow, Scotland

[2]School of Engineering, University of Basilicata, Potenza, Italy

[3]Department of Industrial, Electronic and Mechanical Engineering, University of Roma Tre, Rome, Italy

Correspondence

Carmine Clemente.
Email: carmine.clemente@strath.ac.uk

Abstract

Coregistration is among the most important and challenging tasks when dealing with multiple synthetic aperture radar (SAR) images, especially when they are acquired at different time instants and characterised by low signal to noise power ratio (SNR) that contributes to their coherence reduction. However, even if some technological expedients could be implemented to maintain the same trajectory and to compensate for these inaccuracies during the acquisition campaign, multitemporal SAR images always need additional registration refinements after compression. Usually, to coregister a series of multitemporal SAR images, one of them is selected as the master, and the remainders are separately registered to it. Differently, in this study, a new strategy is developed to jointly coregister a stack of multitemporal SAR images. It is based on the exploitation of the cross-correlations in turn computed from each couple of cross-correlations (a.k.a. cross-cross-correlations) of the extracted patches. By doing so, the method is capable of exploiting also the respective misregistration information between the slaves during the estimation process. In this respect, this methodology is applied to enhance the registration capabilities of the constrained Least Squares (CLS) optimisation method, which instead does not account for the reciprocal information related to the slaves. Several tests are performed on multitemporal airborne-measured SAR data. Obtained results show the effectiveness of the proposed algorithm in terms of achieved root mean square error for images affected by respective rotations also in comparison with the CLS counterpart.

KEYWORDS

correlation methods, image registration, least mean squares methods, synthetic aperture radar

1 | INTRODUCTION

Coregistration of multitemporal synthetic aperture radar (SAR) images is one among the most important steps to be done during the generation of interferograms or other SAR-related products. As a matter of fact, when the acquisition process is repeated over time or it is performed with multiple sensors, it is expected that the acquired images differ somehow from each other as a consequence of the different trajectories followed by the platforms. Even the minor mismatch in trajectories can have a significant effect on the position of the final scene represented, thus affecting final SAR-related products. Therefore, a widely applied solution to this issue consists in performing an image coregistration procedure after the image formation process [1–3]. Coregistration simply consists in aligning the images (dubbed as slaves) with respect to that selected to be the master in order to make each pixel in the couple master-slave refer to the same scatterers in the physical scene.

Two main philosophies have been generally followed in the open literature to achieve the image registration objective [4]: the first family of methods, called feature-based, relies on the identification of the so-called tie-points in the two images that are then coupled to estimate the relative shift among them; the other approaches, also referred to as area-based, exploit the

misalignment information for instance embedded in the two-dimensional (2D) spatial cross-correlation between uniformly extracted patches in the master and slave. It is also worth highlighting that the above mentioned approaches typically perform a rigid translation in both range and azimuth directions of the slave so as to match with its master followed by a resampling of the pixels.

All the above considerations found application in many methodologies and algorithms that have been developed in the last decades [5–19]. Among them, the authors in Ref. [6] exploit geometrical considerations as well as some additional information (e.g. orbital information) to perform an accurate registration of multitemporal and multibaseline images. Moreover, in Refs. [7, 8], the displacement vector field is regularised using a non-linear diffusion process to design frameworks that are capable of providing robust and accurate registrations. References [9–13] are all based on the evaluation of the peak position in the modulus of the 2D cross-correlation of the imagery. More recently, some different methods resorting to a feature-based approach have been also developed, for example, [20–28]. In particular, the authors in Ref. [20] propose a feature-based approach exploiting image segmentation and that benefits of an outliers removal procedure. Moreover, also other methods like [22, 26] propose advanced methods based on SIFT.

When dealing with a multitude of SAR images acquired at different times, the coregistration is performed by setting one image (typically the first acquisition) as the master and the remainder as slaves. Then, each slave is separately coregistered to the master without accounting for a respective displacement with the other slaves. In this study, the idea is to perform a joint estimation of the required parameters considering a unique coregistration of all slaves to the master jointly accounting for the respective displacements among slaves during the estimation process. By doing so, the method is capable of providing a more robust estimate of the involved quantities. Specifically, the method extends the constrained least squares (CLS) algorithm designed in Refs. [17–19] for rotated and translated images using the information extracted from the cross-cross-correlations (i.e., the cross-correlation with a couple of patches cross-correlations) of the same patches centred in the identifying extended targets/areas extracted from all images. Preliminary results of the proposed joint coregistration method have been published in Ref. [29]. Tests conducted using the multitemporal Gotcha Volumetric SAR Data Set V1.0 show the benefits that occur by using the proposed joint coregistration pipeline, which is also in comparison with its standard one-by-one registration counterpart.

1.1 | Notation

We use boldface lower case for vectors $\boldsymbol{a}$ and upper case for matrices $\boldsymbol{A}$. The kth entry of $\boldsymbol{a}$ is denoted by $\boldsymbol{a}(k)$, and the (k, n)-th entry of $\boldsymbol{A}$ is denoted by $\boldsymbol{A}(k, n)$. Then, $\mathbf{diag}(\boldsymbol{a})$ is the diagonal matrix whose diagonal entries are the values in vector $\boldsymbol{a}$, whereas $\boldsymbol{0}$ and $\boldsymbol{1}$ are the vectors with all zeros and all one

entries, respectively. The symbols $\mathbb{R}$ and $\mathbb{C}$ denote the set of real and complex numbers, respectively, and $\mathbb{C}^{K \times N}$ is the Euclidean space of $(K \times N)$-dimensional complex matrices (or vectors if $N = 1$), whereas $\mathbb{S}^N$ is the set of $N \times N$ symmetric matrices. The symbols $(\cdot)^T$ and $(\cdot)^\dagger$ denote the transpose and conjugate transpose operators, respectively, while $|\cdot|$ and $\|\cdot\|$ are the modulus and Euclidean matrix norm, respectively. The curled inequality symbol $\succeq$ is used to indicate generalised matrix inequality: for any $\boldsymbol{A} \in \mathbb{C}^N$, $\boldsymbol{A} \succeq \boldsymbol{0}$ means that $\boldsymbol{A}$ is a positive semi-definite matrix. $\lambda_1(\boldsymbol{A})$, ..., $\lambda_N(\boldsymbol{A})$, with $\lambda_1(\boldsymbol{A}) \geq ... \geq \lambda_N(\boldsymbol{A})$, denote the eigenvalues of $\boldsymbol{A} \in \mathbb{S}^N$, arranged in decreasing order. Furthermore, given $\boldsymbol{B} > \boldsymbol{0}$ and $\boldsymbol{A} \in \mathbb{S}^N$, the generalised eigenvalues of the matrix pair $(\boldsymbol{A}, \boldsymbol{B})$ are given by $\lambda_i(\boldsymbol{A}, \boldsymbol{B}) = \lambda_i(\boldsymbol{B}^{-1/2}\boldsymbol{A}\boldsymbol{B}^{-1/2})$, $i = 1, ..., N$. Finally, $j = \sqrt{-1}$ is the imaginary unit.

2 | MULTITEMPORAL SAR IMAGE COREGISTRATION ALGORITHM

Let us consider the availability of K SAR images representative of the same observed scene acquired at different time instants, $\boldsymbol{I}_k(z) \in \mathbb{C}^{M \times N}$, $k = 0, ..., K - 1$, with $z = x + jy$ the complex variable describing the Cartesian coordinates x and y [30]. Let us select, without loss of generality, the image indexed with $k = 0$ as the master, that is $\boldsymbol{I}_m(z) \in \mathbb{C}^{M \times N}$. Consequently, the remainders $K - 1$ images, $\boldsymbol{I}_{s_k}(z) \in \mathbb{C}^{M \times N}$, $k = 1, ..., K - 1$, are denoted as slaves. By doing so, the effect of pixels translation and rotation of a slave with respect to the master can be defined as

$$\boldsymbol{I}_{s_k}(z) = \boldsymbol{I}_m\left(\frac{z - \delta_k}{\alpha_k}\right) + \boldsymbol{E}_k(z),$$
$$k = 1, ..., K - 1, \tag{1}$$

with $\boldsymbol{E}_k(z)$ denoting the kth error image accounting for noise variations, image decorrelations, and different scattering properties. Moreover, $\delta_k = \delta_{x_k} + j\delta_{y_k}$ is the complex displacement describing the relative shifts, δ_{x_k} and δ_{y_k}, of the generic slave image with respect to the master in both x- and y-direction. Finally, the complex scaling factor $\alpha_k = \gamma_k \exp[j\theta_k]$ is introduced to account for both rotation (through the angle θ_k) and the zooming effect (ruled by γ_k).

The aim of the procedure proposed in this study is to provide an efficient solution in the estimation of the unknown parameters, $\delta_k \in \mathbb{C}$ and $\theta_k \in \mathbb{R}$, enforcing the absence of zooming effect (i.e., setting $\gamma_k = 1$), for all the $K - 1$ slave images. More precisely, the idea is to jointly estimate the quoted parameters that are also accounting for the respective misalignments between the slave images. In this respect, the proposed method is based on the solution of the CLS problem developed in Ref. [17], after a proper selection of the areas of interest in the images as in Ref. [18]. More in detail, once the patches from the master and slaves are extracted, a cross-cross-correlation-based method, devised in Ref. [31] for the delay

estimation for 1-dimensional signals, is applied to obtain all the displacement fields for the slave images in the considered stack with respect to the selected master.

The proposed algorithm is described by the functional scheme as shown in Figure 1 whose main steps are detailed in the following.

The starting input of the algorithm is the image selected to be the master that is used to apply the procedure developed in Ref. [18] to properly select the patches needed for the displacement field evaluation. In particular, the method of Ref. [18] applies a constant false alarm rate [32] detection scheme to the entire image to detect strong reflective areas. The resulting binary detection map is then improved thanks to a clustering and false alarms cancellation procedure. In fact, the clustering based on the use of an order filter allows to improve the shape of the detected object/area exploiting the behaviour of the neighbouring pixels of that under test. Meanwhile, the false alarm cancellation, based on a median filter, is performed to delete all noisy single detections belonging to the map. Once the extended objects are definitely obtained in the master image, their centroids are evaluated as their centre of mass. Then, for each centroid in the master, a patch in its centre is extracted from both the master and all slave images and all possible cross-correlations between these corresponding patches in the K images are computed. The reason for performing the patch detection only on the master image is twofold: from one side it allows to reduce the computation burden with respect to applying the detection process over more images. On the other side, by doing so, the risk of losing a matching between patches in each couple of image is mitigated. Additionally, the cross-correlations between each couple of patch cross-correlations are evaluated before constructing the overall displacement field needed to solve the CLS problem as detailed in Section 2.1. In fact, as shown in Ref. [31] for TDOA estimation, by

exploiting the additional information provided by the cross-cross-correlation, it would be expected that the new method performs better than the classic competitor in the presence of correlated images and high-power noise. In fact, it is interesting to observe that random errors arising in the estimation of the cross-correlation peaks could be reduced since a higher number of equations is employed in searching the pseudosolution of the LS problem. Moreover, the fourth-order correlation can be also seen as a filtering operation on the incoming images. Finally, the procedure is repeated for each patch detected in the master and extracted in all slaves. By doing so, the displacement field is evaluated for each slave as the vector containing the single displacements of each couple of tie-points in the master-slave solving the overall cross-cross-correlations problem.

2.1 | CLS formulation and its solution

The CLS problem designed in Ref. [17] allows the registration of a slave image $I_s(z) \in \mathbb{C}^{M \times N}$, affected by rotation and shift, to a master $I_m(z) \in \mathbb{C}^{M \times N}$ representative of the same observed scene. To do this, the method needs to identify some tie-points (described in Section 2.2) in both the master and slave, here indicated as $z_l = (x_{m,l} + jy_{m,l})$, and $\zeta_l = x_{s,l} + jy_{s,l}$ and $l = 1, \ldots, L$, respectively. Then, the displacement field between them can be obtained as the solution of an over-determined constrained linear system of L equations in 3 unknowns [17], that is,

$$\alpha z_l + \delta = \zeta_l, \; l = 1, \ldots, L, \tag{2}$$

where $\alpha = \gamma e^{j\theta}$ is a complex scalar factor accounting for rotation, described by the rotation angle θ and the zooming factor γ, and $\delta = \delta_x + j\delta_y$ the complex displacement
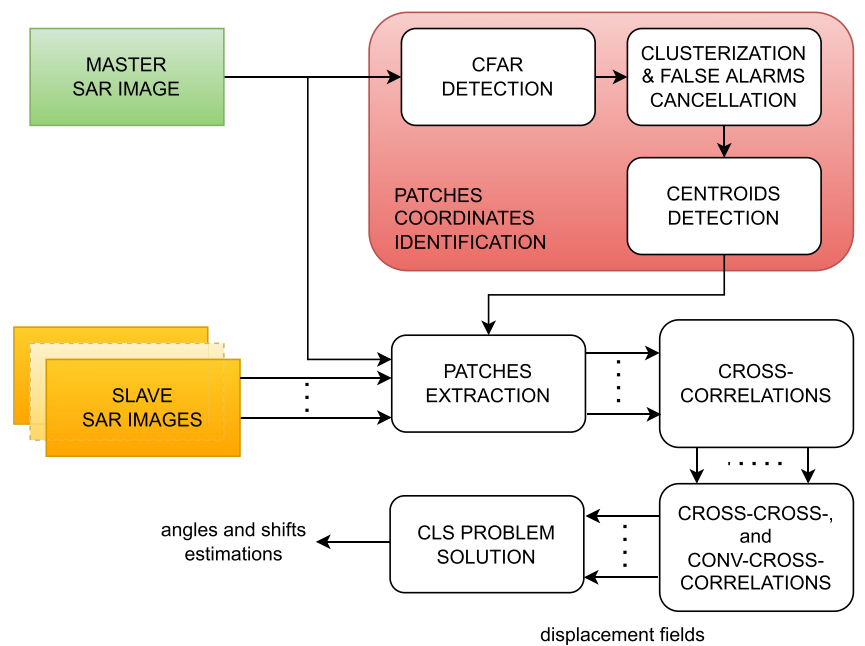
FIGURE 1 Block scheme of the multitemporal synthetic aperture radar images coregistration algorithm based on the use of the cross-cross-correlations.

accounting for horizontal δ_x and vertical δ_y displacements, respectively. Equivalently, Equation (2) can be expressed in a matrix form as

$$\begin{cases} \underset{p}{\arg\min} \|Ap - \mathrm{diag}\,(w)\zeta\|^2 \\ \text{s.t. } p^\dagger Dp - 1 = 0 \end{cases}, \qquad (3)$$

where $p = [\alpha, \delta]^T$ is the vector containing the unknown parameters, and $\zeta = [\zeta_1, \ldots, \zeta_L]^T$ the measurement vector containing the coordinates $\zeta_1, \ldots, \zeta_L$ of the displacement field expressed with respect to the reference system centred at the image centre. Note that in Equation (3), the weighting vector $w = [w_1, \ldots, w_L]^T$ is also considered to differently weigh the impact of each extracted patch in the LS problem.[1] Finally, $A = \mathrm{diag}\,(w)Z$, with

$$Z = \begin{bmatrix} z_1 & 1 \\ \vdots & \vdots \\ z_L & 1 \end{bmatrix}$$

the $L \times 2$ matrix containing the complex coordinates of the tie-points in the master image and

$$D = \begin{bmatrix} 1 & 0 \\ 0 & 0 \end{bmatrix}$$

the constraint matrix in the CLS problem.

As demonstrated in Ref. [17], an optimal solution to Problem (3) can be found resorting to the theory of Ref. [33]. Therefore, assuming that the matrix A is a full column rank, the optimal solution to the CLS is

$$p^\star = \left(A^\dagger A + \beta D\right)^{-1} A^\dagger \mathrm{diag}\,(w)\zeta, \qquad (4)$$

with β solution of $\varphi(\beta) = 0$, $\beta \in \mathcal{I} \subseteq \mathbb{R}$, and $\varphi(\beta) = p^\dagger Dp - 1$. The interval $\mathcal{I}$ consists of all β for which $A^\dagger A + \beta D$ is positive definite, which implies that

$$\beta \in \left(-\frac{1}{\lambda_1(D, A^\dagger A)}, +\infty\right). \qquad (5)$$

The interested reader can refer to [17] for additional details.

2.2 | Displacement field evaluation thorough the use of cross-cross-correlations

A standard procedure to estimate the displacement field (i.e., the values ζ_l, $l = 1, \ldots, L$, contained in the vector ζ) used to form Problem (3) consists in evaluating the position of the

peak in the magnitude of cross-correlation between corresponding patches in the master and slave as

$$[\hat{y}, \hat{x}]_k = \underset{y,x}{\arg\max}\left\{\left|G_{0,k}(y,x)\right|\right\}, \quad k = 1, \ldots, K-1. \qquad (6)$$

where

$$\begin{aligned} G_{0,k}(y,x) &= \sum_{m=0}^{M-1}\sum_{n=0}^{N-1} P_0(m,n)P_{s_k}^*(m-y, n-x), \\ &\quad -(N-1) \le y \le (M-1), \\ &\quad -(N-1) \le x \le (M-1) \end{aligned} \qquad (7)$$

is the spatial cross-correlation of the quoted couple of patches P_0 and P_{s_k} in the master and kth slave, respectively. Note that, in the previous equations we have omitted the subscript s to indicate that x and y are the displacement in the x- and y-direction of the patch associated to a slave image.

Beyond the classic cross-correlation G evaluated with respect to the master, it is possible to consider all possible couples of images (discarding the auto-correlation). In this case, the total number of possible combinations of K images is $Q = (K^2 - K)/2$. Additionally, it would be useful to derive the cross-correlation and convolution (say conv-cross-correlation) between each couple of images of cross-correlations, in order to obtain $T = K^4/4 - K^3/2 - K^2/4 + K/2$ combinations.

The cross-cross-correlation and the conv-cross-correlation (also denoted as flipped cross-cross-correlation) can be, respectively, defined as

$$\begin{aligned} C_{ihlp}\left(\rho_y, \rho_x\right) &= \sum_{y=0}^{M+N-1}\sum_{x=0}^{M+N-1} G_{ih}(y,x)G_{lp}^*\left(y-\rho_y, x-\rho_x\right), \\ &\quad -(M+N-1) \le \rho_y \le (M+N-1), \\ &\quad -(M+N-1) \le \rho_x \le (M+N-1), \\ &\quad i,h,l,p = 0, \ldots, K-1 \ (h > i \text{ and } p > l), \end{aligned} \qquad (8)$$

and

$$\begin{aligned} F_{ihlp}\left(\rho_y, \rho_x\right) &= \sum_{y=0}^{M+N-1}\sum_{x=0}^{M+N-1} G_{ih}(y,x)G_{lp}\left(\rho_y-y, \rho_x-x\right), \\ &\quad -(M+N-1) \le \rho_y \le (M+N-1), \\ &\quad -(M+N-1) \le \rho_x \le (M+N-1), \\ &\quad i,h,l,p = 0, \ldots, K-1 \ (h > i \text{ and } p > l). \end{aligned} \qquad (9)$$

The apex of the magnitude of the cross-cross-correlation, $\left|C_{ihlp}\left(\rho_y, \rho_x\right)\right|$, should be at the index

$$[y_i - y_h - y_l + y_p, x_i - x_h - x_l + x_p],$$

---

[1] Note that, for all the analyses reported in this paper all equal weights are used, that is, $w = 1$. Nevertheless, the optimal selection of the weights (e.g., depending on the image coherency) will be investigated in future works.

while that of $|\boldsymbol{F}_{ihlp}(\rho_y, \rho_x)|$ should be at the index

$$[y_i - y_h + y_l - y_p, x_i - x_h + x_l - x_p].$$

Hence, we can estimate the $K - 1$ displacements in the MMSE sense solving the overdetermined system made by the T equations, consisting of the linear combination of the $2(K - 1)$ unknowns (i.e., $K - 1$ unknowns for each x- and y-coordinate) equal to the index of the maximum of the standard and flipped cross-cross-correlations considered in Equations (8) and (9), that is,

$$[y_i - y_h - y_l + y_p, x_i - x_h - x_l + x_p] = \left[\overline{\rho}_y, \overline{\rho}_x\right]_{ihlp} \quad (10)$$
$$i, h, l, p = 0, \ldots, K - 1 \ (h > i \text{ and } p > l),$$

and

$$[y_i - y_h + y_l - y_p, x_i - x_h + x_l - x_p] = \left[\breve{\rho}_y, \breve{\rho}_x\right]_{ihlp} \quad (11)$$
$$i, h, l, p = 0, \ldots, K - 1 \ (h > i \text{ and } p > l),$$

where

$$\left[\overline{\rho}_y, \overline{\rho}_x\right]_{ihlp} = \underset{\rho_y, \rho_x}{\operatorname{argmax}}\left\{\left|\boldsymbol{C}_{ihlp}\left(\rho_y, \rho_x\right)\right|\right\}, \quad (12)$$

and

$$\left[\breve{\rho}_y, \breve{\rho}_x\right]_{ihlp} = \underset{\rho_y, \rho_x}{\operatorname{argmax}}\left\{\left|\boldsymbol{F}_{ihlp}\left(\rho_y, \rho_x\right)\right|\right\}. \quad (13)$$

Resorting to a compact matrix form, Equations (10) and (11) can be rewritten as

$$\boldsymbol{M}\boldsymbol{U} = \boldsymbol{\Xi}, \quad (14)$$

with

$$\boldsymbol{U} = [\boldsymbol{y}, \boldsymbol{x}] = \begin{bmatrix} y_1 & x_1 \\ \vdots & \vdots \\ y_{K-1} & x_{K-1} \end{bmatrix}, \quad (15)$$

$$\boldsymbol{\Xi} = \left[\boldsymbol{\rho}_y, \boldsymbol{\rho}_x\right]$$

$$= \begin{bmatrix} \overline{\rho}_{y_{0102}} & \overline{\rho}_{x_{0102}} \\ \vdots & \\ \overline{\rho}_{y_{(K-3)(K-1)(K-2)(K-1)}} & \overline{\rho}_{x_{(K-3)(K-1)(K-2)(K-1)}} \\ \breve{\rho}_{y_{0102}} & \breve{\rho}_{x_{0102}} \\ \vdots & \\ \breve{\rho}_{y_{(K-3)(K-1)(K-2)(K-1)}} & \breve{\rho}_{x_{(K-3)(K-1)(K-2)(K-1)}} \end{bmatrix} \quad (16)$$

The model matrix $\boldsymbol{M}$ of size $T \times (K - 1)$ depends only on the number of multitemporal SAR images K and comprises several null elements and some non-zero elements equal to ± 1

and ± 2. More specifically, the values ± 1 are related to measurements where an image is involved in a single operation, for example, one cross-correlation. Whereas, the values ± 2 are related to measurements where an image is involved twice, for example, in both the cross-correlations used in the cross-cross (for readers ease, more details on how to construct the model matrix as well as some practical examples are reported in Appendix 6). For this reason, it can be computed and a-priori stored reducing the computational complexity in real-time algorithms. In fact, the solution to (14) is obtained through the pseudo-inverse of $\boldsymbol{M}$, that is,

$$[\hat{\boldsymbol{y}}, \hat{\boldsymbol{x}}] = \hat{\boldsymbol{U}} = \left(\boldsymbol{M}^T \boldsymbol{M}\right)^{-1} \boldsymbol{M}^T \boldsymbol{\Xi}. \quad (17)$$

Finally, repeating the procedure for all the L patches, the entries of $\hat{\boldsymbol{y}}$ and $\hat{\boldsymbol{x}}$ are used to construct the displacement field of each slave, $\boldsymbol{\zeta}^{(l)}$ and $l = 1, \ldots, L$, needed for the rotation angle and displacement estimation in Equation (3).

Algorithm 1 shows the pseudo-code that summarises the main steps involved in the proposed cross-cross-correlation-based procedure for joint displacement fields estimation. This procedure is hence repeated L times for each patch detected in the master.

Algorithm 1 Pseudo-code for the proposed framework for displacement fields evaluation

1: **Input:** Extracted patches from master $\boldsymbol{P}_0$ and slave images P_{s_k}, $k = 1, \ldots, K - 1$;
2: **Output:** Estimated displacement fields associated with all the slave images $[\hat{\boldsymbol{y}}, \hat{\boldsymbol{x}}]$.
3: **Model Matrix Definition**
4: Compute the model matrix $\boldsymbol{M}$ of size $T \times (K - 1)$;
5: **Measurements Acquisition**
6: Evaluate the cross-correlation estimates through Equation (7) for each couple master-slave and for all the extracted patches;
7: Compute the cross-cross- and conv-cross-correlations through Equations (8) and (9) for each couple of cross-correlations;
8: Perform the measurements of the peaks' positions of the cross-cross-correlations and its flipped version through Equations (12) and (13) and store them in the matrices $\left[\overline{\rho}_y, \overline{\rho}_x\right]_{ihlp}$ and $\left[\breve{\rho}_y, \breve{\rho}_x\right]_{ihlp}$;
9: Construct the measurements matrix $\boldsymbol{\Xi}$ through Equation (16).
10: **Solutions Computation**
11: Compute the solution with the pseudo-inverse of $\boldsymbol{M}$ through Equation (17).

2.3 | Outlier equation cancelation

Once the displacement field is obtained through Equation (17), and consequently, Problem (3) is formalised, the set of equations in it contained can be refined by means of the application of the iterative outlier cancelation procedure developed in Refs. [18, 19]. More precisely, this framework firstly evaluates the absolute error for each entry of the estimated parameters vector $\hat{\boldsymbol{p}}$, namely

$$\boldsymbol{\epsilon} = |\boldsymbol{A}\hat{\boldsymbol{p}} - \text{diag}(\boldsymbol{w})\boldsymbol{\zeta}|, \tag{18}$$

with $|\cdot|$ the absolute value of each element in its vector argument. Then, it rejects all equations that share errors higher than a threshold set according to the so-called median absolute deviation criterion [34, 35]. Finally, the resulting system of the equation (characterised by having a reduced size) is solved to recover the final solution [18, 19].

3 | PERFORMANCE ASSESSMENT

This section is aimed at assessing the performance of the proposed method for the joint coregistration of multitemporal SAR images. Tests are conducted on the challenging full-polarimetric *Gotcha Volumetric SAR Data Set V1.0* [36], characterised by having a full azimuth coverage and eight different elevation angles with images acquired at different time instants. The sensor used for the acquisitions is located on a plane and operates at a carrier frequency of 9.6 GHz with a wide bandwidth of 640 MHz. The observed scene is a car parking containing several civilian vehicles (cars, forklift, and tractor) and also calibration targets. For the conducted study, the aperture was divided into azimuth sub-apertures of 4°, providing approximately equal range-azimuth resolution cells of 23 cm. By doing so, the resulting dataset comprises 90 images (looks) of 501×501 pixels for each of the 8 circular passes (different elevations) in the four polarisations (viz., HH, VV, HV, VH). To better understand the observed scene, Figure 2 depicts the span (expressed in dB) of the full-polarimetric Gotcha SAR image at $0 - 3°$ in azimuth.

In the next tests, without the loss of generality, we focus on the HH polarisation, considering all eight passes of acquisition once the azimuth angle has been fixed; then, the master is chosen to be the image at pass 1, whereas the slaves are those from pass 1–7. Since the Gotcha images provided are already registered to each other, in the devised tests, each slave is clockwise or counterclockwise rotated by an angle θ_k, $k = 1, \ldots, K - 1$, followed by a nearest neighbour interpolation to compensate the non-integer translation of the pixels.

The analyses are conducted considering as the figure of merit the root mean square error (RMSE) of the estimated angles

$$\text{RMSE} = \sqrt{\mathbb{E}\left[\left\|\boldsymbol{\theta} - \hat{\boldsymbol{\theta}}\right\|^2\right]}, \tag{19}$$
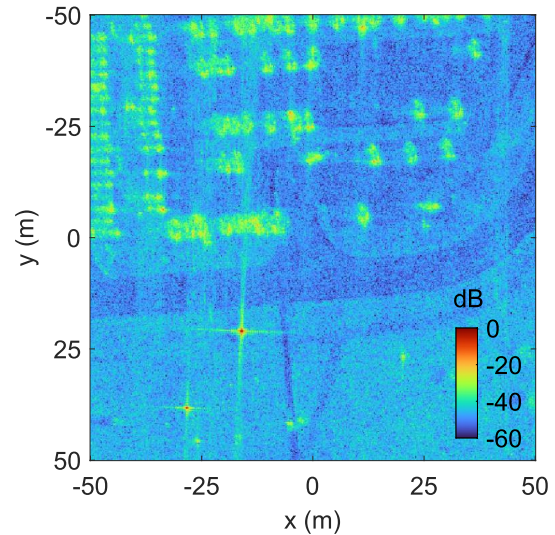

FIGURE 2 Span (dB) of the full-polarimetric Gotcha synthetic aperture radar image at 0° azimuth.

where $\boldsymbol{\theta} = [\theta_1, \ldots, \theta_7]^T$ is the vector containing the seven angles to estimate, whereas $\hat{\boldsymbol{\theta}}$ is the vector containing their estimates. Now, because of the lack of a closed form expression for the RMSE, it is numerically evaluated by resorting to the Monte Carlo simulation procedure. More precisely, at each Monte Carlo trial, $i = 1, \ldots, M_c$ (with M_c the number of runs), each slave image is rotated by an angle θ_k, $k = 1, \ldots, 7$, randomly chosen in the interval $[-2°, 2°]$.

The first test aims at empirically evaluating the optimum choice for the patch size. In fact, the size of the patches extracted from the imagery will directly have an impact on the final coregistration performance. This size can be a-priori set based on considerations about the overall image extent as well as the size of targets that are expected to be in it contained. Hence, Figure 3 shows the RMSE (expressed in °) versus the patch size, having considered, without the loss of generality and square shaped patches. The curves are related to the sequence of eight images for three different azimuth angles, viz., 0°, 176°, and 356°. Moreover, the RMSE is evaluated over a total of $M_c = 100$ Monte Carlo runs chosen from the true rotation angles as described above.

As expected, the three curves show a coherent behaviour of each other. In fact, the RMSE is higher when the patch size is chosen to be very small (in this case, possible extended targets are spread over more patches) and also when it is chosen to be too much large (in this case, more than one target could be contained in the same patch). In particular, from the graph, it can be assured that the optimal patch size for these images is between 18×18 and 32×32 pixels.

For the above mentioned reason, in the successive tests, we set the patch size equal to 25×25 and 30×30 pixels. Therefore, Figures 4 and 5 compare the proposed method, indicated as joint CLS (JCLS), with the CLS of Ref. [18] by evaluating their achieved RMSE values for each slave image. The tests are again conducted for the same settings as in the previous analyses with the results achieved for the three
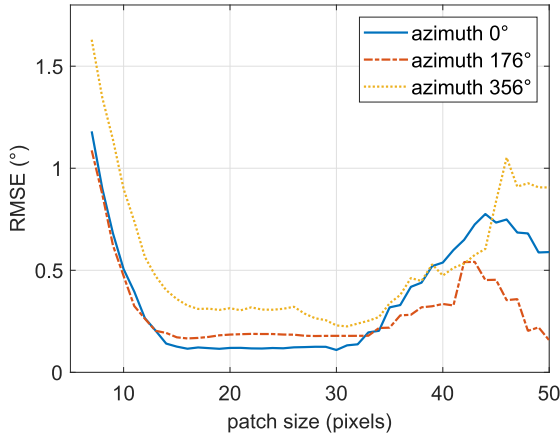
FIGURE 3 Root mean square error (°) versus the patch size for three sequences of 8 synthetic aperture radar images acquired at different azimuth angles, viz. 0°, 176°, and 356°. A total of 100 Monte Carlo runs are performed randomly by selecting the rotation angles in the interval [−2°, 2°].

different azimuth angles (viz. 0°, 176°, and 356°) as shown in the respective subplots.

The graphical bars emphasise the superiority of the JCLS in jointly estimating the involved rotation angles. In fact, even if for some specific images the RMSE of the JCLS is slightly higher than that of the CLS, it gains much more for the others. In fact, the RMSE values shown by the JCLS are mostly homogeneous, whereas those of the CLS are strongly unbalanced. Therefore, we can conclude that the JCLS tends to mitigate the rotation angle estimation performance error to provide a more balanced situation for the involved image stack.

3.1 | Master image and number of slaves selection

For a further evaluation of the most favourable choice for the patch size and the minimum number of slave images needed, the experiment is repeated by choosing the images from acquisition passes 0–7 to be the master images, as well as choosing different number of slave images for each experiment. This test allows also to show the robustness of the proposed framework with respect to which image is selected to be the master.

The behaviour of the curves obtained is consistent with the first experiment, where the master image was the one from acquisition pass 1, and the rest acquisition images were chosen to be the slaves. The RMSE decreases as the patch size increases until the optimal patch size is reached, increasing again thereafter. Figure 6 shows the evolution of the RMSE, in degrees, versus the patch size when the master is the image from pass 1 with three different number of slaves configurations. The RMSE becomes smaller as the number of slaves grows, the maximum values are going from 2.95° when only one slave is taken into account, to 2° when 6 slaves are considered. Compared to the results shown in Figure 3, the difference is
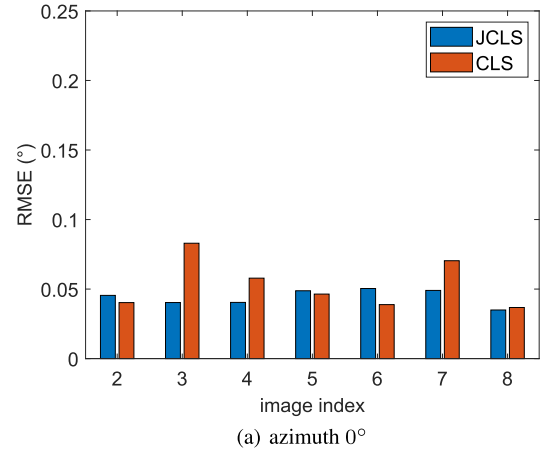
(a) azimuth 0°
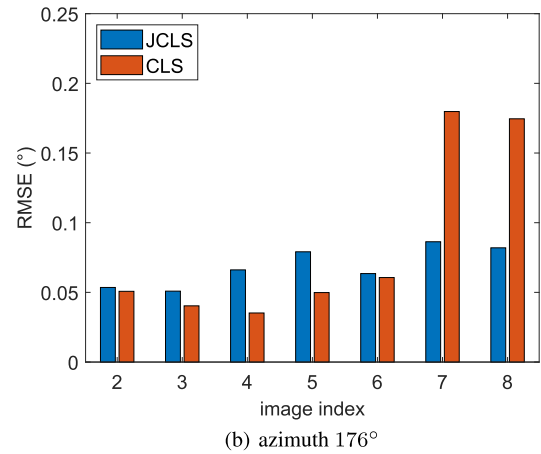
(b) azimuth 176°
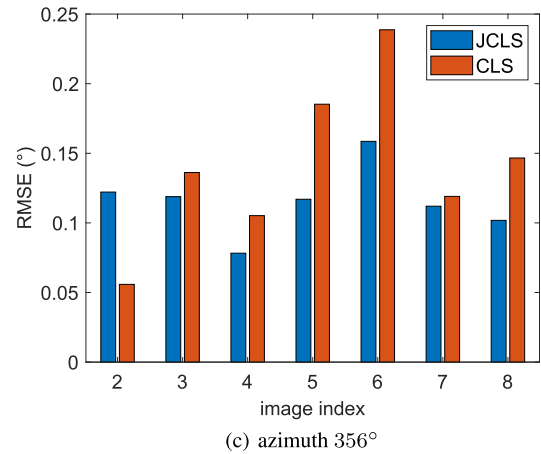
(c) azimuth 356°

FIGURE 4 Root mean square error (°) for each slave of the JCLS and constrained least squares algorithms. The patch size is set to 25 × 25 pixels and subplots refer to 8 synthetic aperture radar images acquired at eight different elevations (marked by the image index). Moreover, three different tests are conducted fixing the azimuth angles to (a) 0°, (b) 176°, and (c) 356°. A total of 100 Monte Carlo runs is performed randomly selecting the rotation angles in the interval [−2°, 2°].

quite noteworthy. The RMSE when 7 slaves are considered, when the patch size is between 25 × 25 and 30 × 30, is under 0.5°. This behaviour has been proven to be uniform across experiments performed over the 8 acquisition passes.
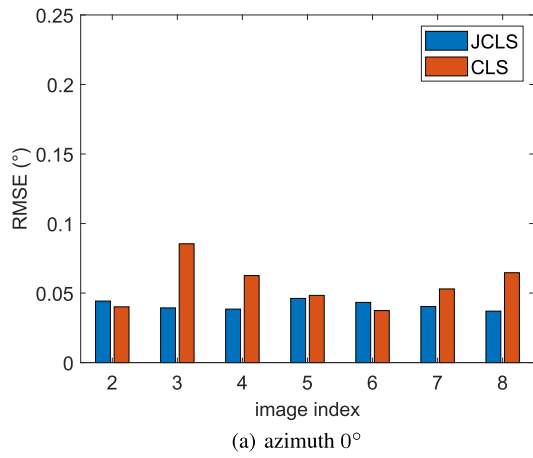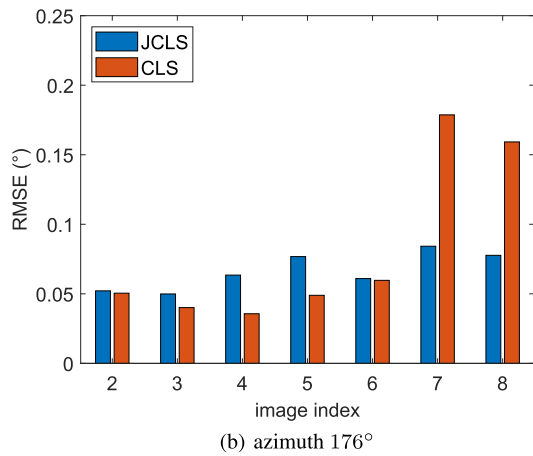
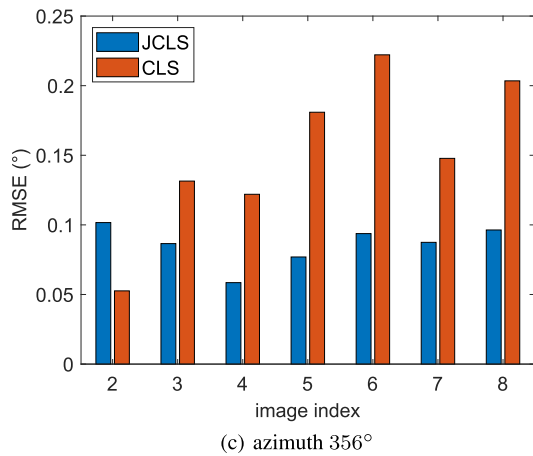**FIGURE 5**   Root mean square error (°) for each slave of the JCLS and constrained least squares algorithms. The patch size is set to 30 × 30 pixels and subplots refer to 8 synthetic aperture radar images acquired at eight different elevations (marked by the image index). Moreover, three different tests are conducted fixing the azimuth angles to (a) 0°, (b) 176°, and (c) 356°. A total of 100 Monte Carlo runs are performed randomly by selecting the rotation angles in the interval [−2°, 2°].

FIGURE 6   Root mean square error (°) versus the patch size for three configurations of the Master image (at pass 1) and different number of slaves acquired at different azimuth angles, 0°, 176°, and 356°. (a) shows the result for a single slave image, (b) the evolution with 4 slave images, and (c) the result for 6 slave images. A total of 100 Monte Carlo runs are performed randomly by selecting the rotation angles in the interval [−2°, 2°].

It can be concluded that the number of slaves cannot be reduced without compromising the performance of the algorithm. This is not surprising observing that the JCLS algorithm experiences a wide reduction in the number of equations as the number of slave decreases. From Figure 6, it can be seen that the optimal patch size lies around 30 × 30 pixels, in accordance to the results shown in Figure 3.
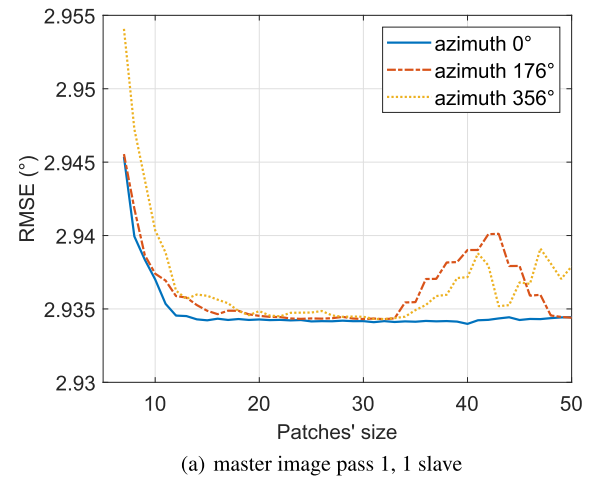
(a) master image pass 4, 1 slave
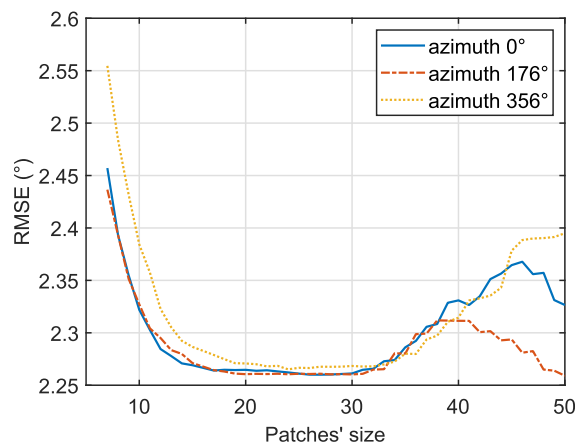
(b) master image pass 4, 4 slaves
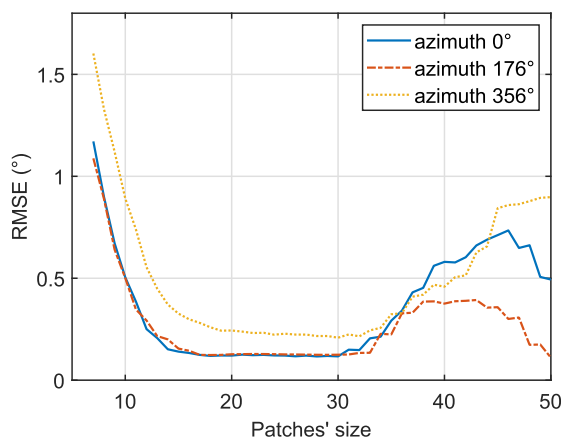
(c) master image pass 4, 7 slaves

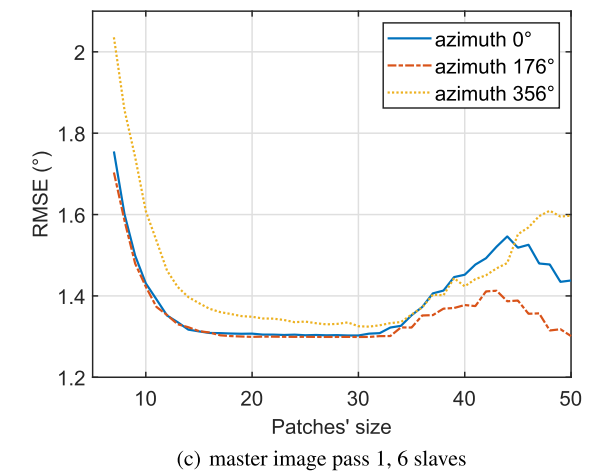**FIGURE 7** Root mean square error (°) versus the patch size for three configurations of the Master image (at pass 4) and different number of slaves acquired at different azimuth angles, 0°, 176°, and 356°. (a) shows the result for a single slave image, (b) the evolution with 4 slave images, and (c) the result for 7 slave images. A total of 100 Monte Carlo runs are performed randomly by selecting the rotation angles in the interval [−2°, 2°].

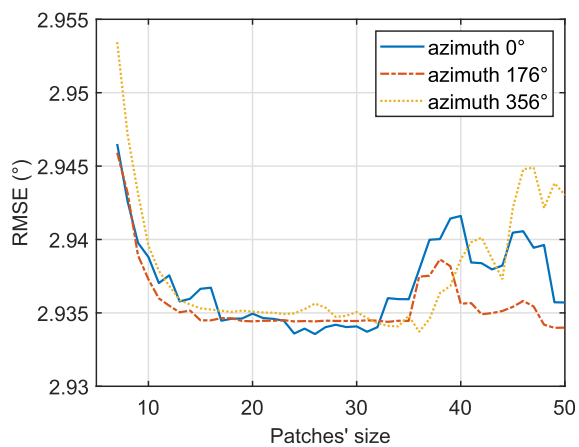(a) master image pass 6, 3 slaves
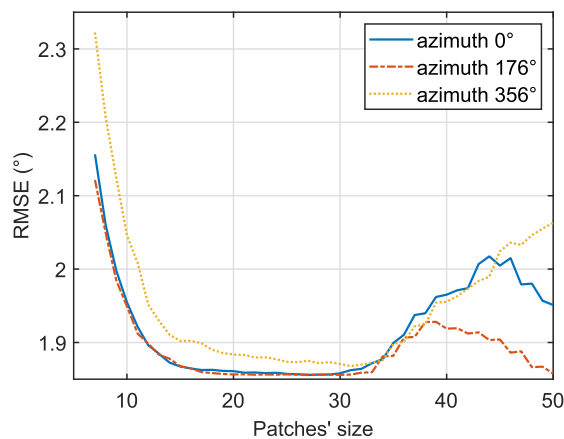
(b) master image pass 6, 5 slaves
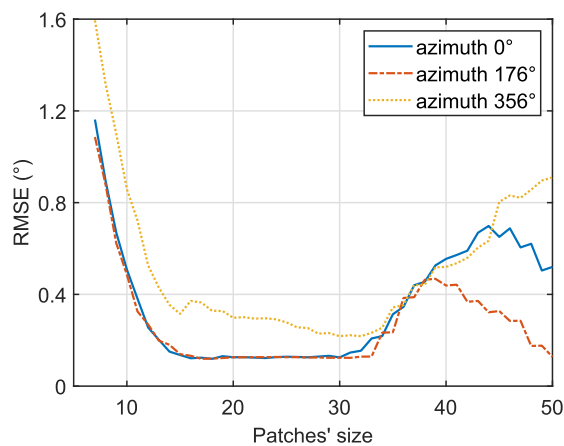
(c) master image pass 6, 7 slaves

FIGURE 8 Root mean square error (°) versus the patch size for three configurations of the Master image (at pass 6) and different number of slaves acquired at different azimuth angles, 0°, 176°, and 356°. (a) shows the result for three slave images, (b) the evolution with 5 slave images, and (c) the result for 7 slave images. A total of 100 Monte Carlo runs are performed randomly by selecting the rotation angles in the interval [−2°, 2°].

To show the consistency of the results of the experiments over different configurations of the master image and number of slaves, three different examples are presented next. In

Figure 7, the case where the master image is taken from pass number four is shown for 3 different number of slave images. Results are presented for one, four, and seven slave images. It

FIGURE 9 Root mean square error (°) versus the patch size for three configurations of Master image (at pass 8) and different number of slaves acquired at different azimuth angles, 0°, 176°, and 356°. (a) shows the result for two slave images, (b) the evolution with 6 slave images, and (c) the result for 7 slave images. A total of 100 Monte Carlo runs are performed randomly by selecting the rotation angles in the interval [−2°, 2°].
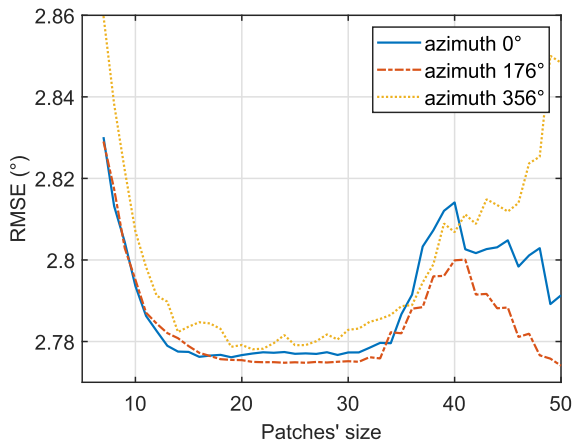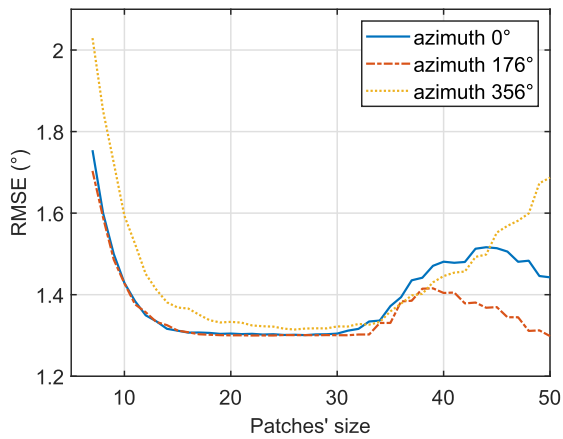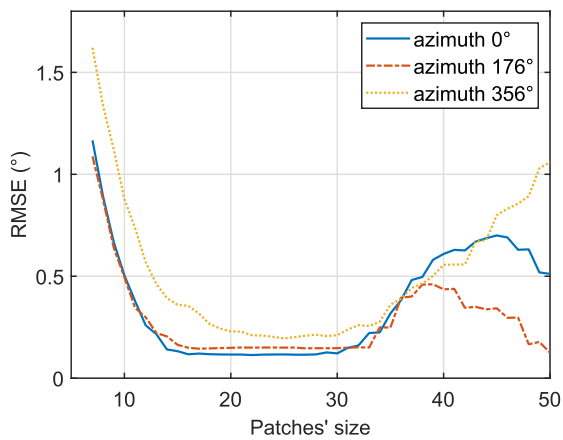
can be seen that the RMSE (°) decreases as the patch number becomes bigger until it reaches the optimal patch size, and at around 30 × 30 pixels, it then increases again. The same trend as before is observed when taking into account the different number of slave images selected. The RMSE decreases as the number of slaves increases.

The second example can be seen in Figure 8, where the image from pass 6 has been taken as the master image. Again, the results follow a similar trend, obtaining lower RMSE (°) as the number of slaves increases and reaches the optimal patch size at around 30 × 30 pixels. In this case, the number of slave images is chosen to be three, five, and seven. For the last example, depicted in Figure 9, the image from the last pass has been taken as the master image, and two, six, and eight slaves have been chosen to illustrate the three different cases. Once again, the three graphs present a similar behaviour compared to the examples seen before: as the number of slaves grows, the RMSE decreases, and for the three cases, the optimal patch size is around 30 × 30 pixels, which is consistent with all the experiments performed.

4 | CONCLUSIONS

This paper has focused on the design of new coregistration algorithm for multitemporal SAR images. The core of the devised method is the joint estimation of the registration parameters for all slave images, namely accounting at the design stage the respective displacements between slaves. Based on the exploitation of the cross-cross-correlations, the derived method is capable of ensuring a more robust behaviour of the registration algorithm for all the involved slave images in the considered stack. Additionally, the method can be considered a fast-algorithm thanks to the closed-form solution of the pseudo-inverse of the model matrix and the fast computation of the cross-correlation by means of the exploitation of the properties of the fast Fourier transform. Results conducted on airborne real-recorded data have demonstrated the validity of the devised model, which is also in comparison with its counterpart non-accounting for a joint registration. Possible future research tracks might regard tests of the developed framework also on spaceborne SAR data.

AUTHOR CONTRIBUTIONS
Laura Parra Garcia: Formal analysis; investigation; methodology; software; validation; writing—original draft. **Luca Pallotta**: Conceptualisation; data curation; formal analysis; methodology; software; supervision; validation; writing—original draft; Writing—review and editing. **Carmine Clemente**: Conceptualisation; data curation; methodology; supervision; validation; writing—original draft; writing—review and editing. **Gaetano Giunta**: Conceptualisation; methodology; supervision; writing—review and editing. **John J. Soraghan**: Conceptualisation; supervision; writing—review and editing.

CONFLICT OF INTEREST STATEMENT
The authors declare that they have no conflict of interests.

DATA AVAILABILITY STATEMENT

The data that support the findings of this study are openly available in at https://www.sdms.afrl.af.mil/index.php?collection=gotcha.

ORCID

Luca Pallotta ![ORCID] https://orcid.org/0000-0002-6918-0383
Carmine Clemente ![ORCID] https://orcid.org/0000-0002-6665-693X

REFERENCES

1. Olmsted, C.: Alaska SAR Facility Scientific SAR User's Guide. Alaska SAR Facility Tech Rep ASF-SD-003 (1993)
2. Richards, M.A.: Fundamentals of Radar Signal Processing. Tata McGraw-Hill Education (2005)
3. Moreira, A., et al.: A tutorial on synthetic aperture radar. IEEE Geoscience and Remote Sensing Magazine 1(1), 6–43 (2013). https://doi.org/10.1109/mgrs.2013.2248301
4. Tondewad, P.S., Dale, M.P.: Remote sensing image registration methodology: review and discussion. Procedia Comput. Sci. 171, 2390–2399 (2020). https://doi.org/10.1016/j.procs.2020.04.259
5. Scheiber, R., Moreira, A.: Coregistration of interferometric SAR images using spectral diversity. IEEE Trans. Geosci. Rem. Sens. 38(5), 2179–2191 (2000). https://doi.org/10.1109/36.868876
6. Sansosti, E., et al.: Geometrical SAR image registration. IEEE Trans. Geosci. Rem. Sens. 44(10), 2861–2870 (2006). https://doi.org/10.1109/tgrs.2006.875787
7. Ceccarelli, M., et al.: Image registration using non-linear diffusion. In: IEEE International Geoscience and Remote Sensing Symposium (IGARSS) 5, pp. 220–223 (2008)
8. Borzí, A., et al.: Robust registration of satellite images with local distortions. In: IEEE International Geoscience and Remote Sensing Symposium (IGARSS) 3, pp. III.251–III.254 (2009)
9. Peterson, E.H., et al.: Registration of multi-frequency SAR imagery using phase correlation methods. In: IEEE International Geoscience and Remote Sensing Symposium (IGARSS), pp. 3708–3711 (2011)
10. Li, D., Zhang, Y.: A fast offset estimation approach for InSAR image subpixel registration. Geosci. Rem. Sens. Lett. IEEE 9(2), 267–271 (2011). https://doi.org/10.1109/lgrs.2011.2166752
11. Li, D., Zhang, Y.: A fast normalized cross-correlation algorithm for InSAR image subpixel registration. In: 3rd IEEE International Asia-Pacific Conference on Synthetic Aperture Radar (APSAR), pp. 1–4 (2011)
12. Wang, Y., Yu, Q., Yu, W.: An improved normalized cross correlation algorithm for SAR image registration. In: IEEE International Geoscience and Remote Sensing Symposium (IGARSS), pp. 2086–2089 (2012)
13. Zhang, Z., et al.: A large width SAR image registration method based on the complex correlation function. In: IEEE International Geoscience and Remote Sensing Symposium (IGARSS), pp. 6476–6479 (2016)
14. Zou, W., Chen, L.: Determination of optimum tie point interval for SAR image coregistration by decomposing autocorrelation coefficient. IEEE Trans. Geosci. Rem. Sens. 57(7), 5067–5084 (2019). https://doi.org/10.1109/tgrs.2019.2896383
15. Ma, Z., et al.: Minimum spanning tree Co-registration approach for time-series sentinel-1 TOPS data. IEEE J. Sel. Top. Appl. Earth Obs. Rem. Sens. 12(8), 3004–3013 (2019). https://doi.org/10.1109/jstars.2019.2920717
16. Pallotta, L., Giunta, G., Clemente, C.: Subpixel SAR image registration through parabolic interpolation of the 2-D cross correlation. IEEE Trans. Geosci. Rem. Sens. 58(6), 4132–4144 (2020). https://doi.org/10.1109/tgrs.2019.2961245
17. Pallotta, L., Giunta, G., Clemente, C.: SAR image registration in the presence of rotation and translation: a constrained least squares approach.

18. Geosci. Rem. Sens. Lett. IEEE 18(9), 1595–1599 (2021). https://doi.org/10.1109/lgrs.2020.3005198
18. Pallotta, L., et al.: SAR coregistration by robust selection of extended targets and iterative outlier cancellation. Geosci. Rem. Sens. Lett. IEEE 19(4501405), 1–5 (2022). https://doi.org/10.1109/lgrs.2021.3132661
19. Pallotta, L., et al.: Coregistration method for rotated/shifted FOPEN SAR images. In: IEEE International Geoscience and Remote Sensing Symposium (IGARSS), pp. 2454–2457 (2022)
20. Goncalves, H., Corte-Real, L., Goncalves, J.A.: Automatic image registration through image segmentation and SIFT. IEEE Trans. Geosci. Rem. Sens. 49(7), 2589–2600 (2011). https://doi.org/10.1109/tgrs.2011.2109389
21. Song, Z., Zhou, S., Guan, J.: A novel image registration algorithm for remote sensing under affine transformation. IEEE Trans. Geosci. Rem. Sens. 52(8), 4895–4912 (2013)
22. Dellinger, F., et al.: SARSIFT: a SIFT-like algorithm for SAR images. IEEE Trans. Geosci. Rem. Sens. 53(1), 453–466 (2015). https://doi.org/10.1109/tgrs.2014.2323552
23. Zeng, L., et al.: Polar scale-invariant feature transform for synthetic aperture radar image registration. Geosci. Rem. Sens. Lett. IEEE 14(7), 1101–1105 (2017). https://doi.org/10.1109/lgrs.2017.2698450
24. Fan, J., et al.: SAR image registration using multiscale image patch features with sparse representation. IEEE J. Sel. Top. Appl. Earth Obs. Rem. Sens. 10(4), 1483–1493 (2017). https://doi.org/10.1109/jstars.2016.2628911
25. Paul, S., Pati, U.C.: A block-based multifeature extraction scheme for SAR image registration. Geosci. Rem. Sens. Lett. IEEE 15(9), 1387–1391 (2018). https://doi.org/10.1109/lgrs.2018.2842921
26. Paul, S., Pati, U.C.: SAR image registration using an improved SAR-SIFT algorithm and delaunay-triangulation-based local matching. IEEE J. Sel. Top. Appl. Earth Obs. Rem. Sens. 12(8), 2958–2966 (2019). https://doi.org/10.1109/jstars.2019.2918211
27. Yao, G., et al.: Registering oblique SAR images based on complementary integrated filtering and multilevel matching. IEEE J. Sel. Top. Appl. Earth Obs. Rem. Sens. 12(12), 3445–3457 (2019). https://doi.org/10.1109/jstars.2019.2929405
28. Xiong, X., et al.: Robust SAR image registration using rank-based ratio self-similarity. IEEE J. Sel. Top. Appl. Earth Obs. Rem. Sens. 14, 2358–2368 (2021). https://doi.org/10.1109/jstars.2021.3055023
29. Pallotta, L., et al.: A joint coregistration of rotated multitemporal SAR images based on the cross-cross-correlation. In: IET International Conference on Radar Systems, Edinburgh, 22–24 (2022)
30. Giunta, G., Mascia, U.: Estimation of global motion parameters by complex linear regression. IEEE Trans. Image Process. 8(11), 1652–1657 (1999). https://doi.org/10.1109/83.799894
31. Pallotta, L., Giunta, G.: Accurate delay estimation for multisensor passive locating systems exploiting the cross-correlation between signals cross-correlations. IEEE Trans. Aero. Electron. Syst. 58(3), 2568–2576 (2022). https://doi.org/10.1109/taes.2021.3116927
32. El-Darymli, K., et al.: Target detection in synthetic aperture radar imagery: a state-of-the-art survey. J. Appl. Remote Sens. 7(1), 071598 (2013). https://doi.org/10.1117/1.jrs.7.071598
33. More', J.J.: Generalizations of the trust region subproblem. Optim. Methods Software 2(3-4), 189–209 (1993). https://doi.org/10.1080/10556789308805542
34. Leys, C., et al.: Detecting outliers: do not use standard deviation around the mean, use absolute deviation around the median. J. Exp. Soc. Psychol. 49(4), 764–766 (2013). https://doi.org/10.1016/j.jesp.2013.03.013
35. Fitriyah, H., Budi, A.S.: Outlier detection in object counting based on hue and distance transform using median absolute deviation (MAD). In: International Conference on Sustainable Information Engineering and Technology (SIET), pp. 217–222 (2019)
36. Ertin, E., et al.: 'GOTCHA experience report: three-dimensional SAR imaging with complete circular apertures'. In: Algorithms for Synthetic Aperture Radar Imagery XIV, vol. 6568. International Society for Optics and Photonics (2007).656802

APPENDIX

A.1 | Detailed procedure for cross-cross-correlation model matrix construction

The model matrix M of size $T \times (K - 1)$ can be constructed following the procedure described in [31]. It starts considering all possible cross-cross-correlations C_{ihlp} that are sequentially re-numbered by the index r with $1 \leq r \leq T/2$. The four corresponding vectors of size $T/2$, I_1, I_2, I_3, and I_4 containing respectively the values assumed by the indices i, h, l, p associated with the rth cross-cross-correlation, are hence introduced. Then, starting from $M = 0$, the (r, c)-th element of M is obtained adding $+1$ if $c = I_1(r)$ or $c = I_4(r)$ and -1 if $c = I_2(r)$ or $c = I_3(r)$. The same four vectors of indices are used for the flipped cross-cross-correlations $F_{ihlp} = C_{ihpl}$ to fill the elements $T/2 + 1 \leq r \leq T$ of M, after switching the rule by adding $+1$ if $c = I_1(r)$ or $c = I_3(r)$, and -1 if $c = I_2(r)$ or $c = I_4(r)$.

In the following, some numerical examples are reported to help the reader in understanding the above procedure. In particular, assuming the availability of $K = 3$ SAR images, the resulting $Q = 3$ cross-correlations are $\{G_{01}, G_{02}, G_{12}\}$. Then, the $T = 6$ normal and flipped cross-cross-correlations are $\{C_{0102}, C_{0112}, C_{0212}\}$ and $\{F_{0102}, F_{0112}, F_{0212}\}$, respectively. As a consequence the four vectors containing the subscripts of C and F are

$$I_1 = \begin{bmatrix} 0 \\ 0 \\ 0 \end{bmatrix}, \quad I_2 = \begin{bmatrix} 1 \\ 1 \\ 2 \end{bmatrix}, \quad I_3 = \begin{bmatrix} 0 \\ 1 \\ 1 \end{bmatrix}, \quad \text{and} \quad I_4 = \begin{bmatrix} 2 \\ 2 \\ 2 \end{bmatrix}.$$

Applying the above-described procedure, the 6×3 model matrix results to be equal to

$$M = \begin{bmatrix} -1 & 1 \\ -2 & 1 \\ -1 & 0 \\ -1 & -1 \\ 0 & -1 \\ 1 & -2 \end{bmatrix}.$$

Similarly, for $K = 4$ SAR images, there are $Q = 6$ cross-correlations, that is, $\{G_{01}, G_{02}, G_{03}, G_{12}, G_{13}, G_{23}\}$. As a consequence $T = 30$ (i.e., 15 cross-cross-correlations and 15 flipped cross-cross-correlations). Hence, the four index vectors of size equal to 15 are

$$I_1 = \begin{bmatrix} 0 \\ 0 \\ 0 \\ 0 \\ 0 \\ 0 \\ 0 \\ 0 \\ 0 \\ 0 \\ 0 \\ 0 \\ 1 \\ 1 \\ 1 \end{bmatrix}, \quad I_2 = \begin{bmatrix} 1 \\ 1 \\ 1 \\ 1 \\ 1 \\ 2 \\ 2 \\ 2 \\ 2 \\ 3 \\ 3 \\ 3 \\ 2 \\ 2 \\ 3 \end{bmatrix}, \quad I_3 = \begin{bmatrix} 0 \\ 0 \\ 1 \\ 1 \\ 2 \\ 0 \\ 1 \\ 1 \\ 2 \\ 1 \\ 1 \\ 2 \\ 1 \\ 2 \\ 2 \end{bmatrix}, \quad \text{and} \quad I_4 = \begin{bmatrix} 2 \\ 3 \\ 2 \\ 3 \\ 3 \\ 3 \\ 2 \\ 3 \\ 3 \\ 2 \\ 3 \\ 3 \\ 3 \\ 3 \\ 3 \end{bmatrix}.$$

Again, applying the above-described procedure, the 30×4 model matrix results to be equal to

$$M = \begin{bmatrix} -1 & 1 & 0 \\ -1 & 0 & 1 \\ -2 & 1 & 0 \\ -2 & 0 & 1 \\ -1 & -1 & 1 \\ 0 & -1 & 1 \\ -1 & 0 & 0 \\ -1 & -1 & 1 \\ 0 & -2 & 1 \\ -1 & 1 & -1 \\ -1 & 0 & 0 \\ 0 & -1 & 0 \\ 0 & -1 & 1 \\ 1 & -2 & 1 \\ 1 & -1 & 0 \\ -1 & -1 & 0 \\ -1 & 0 & -1 \\ 0 & -1 & 0 \\ 0 & 0 & -1 \\ -1 & 1 & -1 \\ 0 & -1 & -1 \\ 1 & -2 & 0 \\ 1 & -1 & -1 \\ 0 & 0 & -1 \\ 1 & -1 & -1 \\ 1 & 0 & -2 \\ 0 & 1 & -2 \\ 2 & -1 & -1 \\ 1 & 0 & -1 \\ 1 & 1 & -2 \end{bmatrix}.$$